Investigation of mechanical properties of garnet structured Li₇La₃Zr₂O₁₂ under Al³⁺ and Ta⁵⁺ co-substitutions

Roland Sandt^{a,c}, Yaxue Wang^a, Robert Spatschek^{a,b}

^aStructure and Function of Materials, Institute of Energy and Climate Research (IEK-2), Forschungszentrum Jülich GmbH, 52425 Jülich, Germany ^bJARA-ENERGY, 52425 Jülich, Germany ^cCorresponding author: r.sandt@fz-juelich.de

Abstract

The influence of co-substitutions on the structural and mechanical properties of garnet structured $\rm Li_7La_3Zr_2O_{12}$ (LLZO) is investigated. Ab initio simulations of the cubic phase under Al and Ta substitutions are performed for an analysis of substitution dependencies on lattice constants, elastic moduli and hardness. The use of the differential effective medium theory methods enables a scale bridging description towards porous LLZO, with a 27 % decay of Young's modulus for a porosity of 10%, compared to dense LLZO.

Keywords: Solid state battery, Electrolyte, Mechanical Properties, Density functional theory, Machine Learning, Pores

1. Introduction

Li-based all solid state batteries (ASSBs) are promising next generation batteries due to their high energy densities, high cycle life, low self-discharge rate and their improved safety behaviour [1, 2, 3, 4, 5]. The absence of liquid electrolytes prevents the cell from leakage and allows an effective usage as a modern battery in electric vehicles and other battery power driven products. However, downsides are still present like the disadvantageous volume expansion of solid battery components during usage and production [3, 4, 6]. Arising stresses and deformations can lead to instabilities and limitation of lifetime, what makes the knowledge of the mechanical behaviour a crucial part of actual research. Another important problem is the Li metal dendrite

growth or rather intrusion [3, 7, 8, 9] inside the electrolyte and therefore occuring short circuits, which can lead to premature and sudden degradation. A recent study by Fincher et al. showed that the dendrite propagation in solid-state batteries can be controlled and deflected by an imposed stress, where a critical stress of around 150 MPa can prevent short circuits [10]. McConohy et al. found out that the main reason for lithium intrusions are localized microstructural defects and cracks within the electrolyte, whose propagation direction can also be controlled mechanically [7]. Therefore, the knowledge of the solid electrolyte's mechanical properties is crucial for an effective usage and production. However, the choice of a suitable solid electrolyte, which determines the performance of the battery, is also important, where Li₇La₃Zr₂O₁₂ (LLZO) is a promising candidate. LLZO is an oxide with high Li-ion conductivity and chemical stability in combination with lithium metal [1, 4, 11]. A thermodynamically stable tetragonal phase with poor Li-ion conductivity [12, 13] exists, whereas the highly conductive cubic phase is desired, which is unstable at ambient temperature [12, 14]. Here, substitutions of different aliovalent elements are an effective way to stabilize the desired cubic phase, where substitutions with Al³⁺, Ta⁵⁺ and Ga³⁺ show good results [13, 14, 15, 16]. Experimentally, combined substitutions with Ta⁵⁺ and Ga³⁺ lead to higher ionic conductivity [13]. Nonemacher et al. [17] investigated experimentally and theoretically single substitutions of Al and Ta in LLZO and their influence on microstructure and mechanical properties.

In this work, we stabilize the cubic phase via combined substitutions of Al and Ta, where benefits of both dopants are exploited and the mechanical behaviour is investigated. Both dopants tantalum (Ta) and aluminium (Al) stabilize the cubic phase, however Al blocks lithium pathways [18], what compensates the increased ionic conductivity, while for Ta substitutions beneficial ionic conductivities are found [19], but the material's costs are also increased [17]. Shin et al. showed the fast stabilization of the cubic phase in co-substituted LLZO and the overcoming of the mentioned blocking effect [20].

Here, the determination of the mechanical properties occurs via density functional theory (DFT) simulations, where a good agreement between experiments and simulations was found for single substitutions in LLZO [17]. Research was also done in respect to the computation of elastic properties of LLZO with Al and Ta single substitutions via DFT simulations [21].

However, DFT calculations of LLZO lead to a high computational demand due to the large number of atoms inside the unit cell (around 190

atoms), a large number of possible substitution sites and the required high precision simulation parameters, in particular energy cutoff and the stopping criteria for electronic and ionic self-consistency loop. Therefore, an acceleration is strongly desired to increase the efficiency and to lower the necessary number of DFT runs and in the end to save energy and computing time. Apart from prescreening techniques for the identification of most favorable lattice site occupations based on an estimation of the electrostatic interaction energy [17], we present here additionally machine learning techniques for obtaining optimized predictions for the ion positions. In general, artificial intelligence, especially machine learning (ML) represents an important part in research, where data sets are analyzed efficiently and workflows and calculations are accelerated drastically. In the field of battery research, ML approaches and models are widely used for example for the prediction of battery lifetime [22]. A common ML method are artificial neural networks (ANNs), which are based on layers and nodes as "neurons" to mimic the human brain and are used to solve prediction, classification and recognition tasks [22, 23, 24, 25]. The optimization via ML methods inside ab initio DFT simulation workflows is a current topic and studies focused on the automatically generation of force fields [26], the improvement of chemical accuracy [27] or the prediction of further physical quantities and properties [28, 29, 30].

LLZO used for battery applications is typically polycrystalline and porous, which has influence on the elastic and mechanical properties [17, 31, 32]. Experiments on LLZO have shown that the results of indentation tests are influenced by the porosity regarding different indentation depths and corresponding loads [17], indicating the multi-scale nature of the material. Thus, it is crucial to extend the electronic structure modeling level to the microstructure scale for a parameter free prediction of the coarse-grained mechanical properties.

2. Methods

2.1. Calculation of the mechanical properties

For all simulations density functional theory (DFT) is used, as implemented in the Vienna ab initio simulation package (VASP) [33] with plane wave basis set and the projector augmented wave (PAW) method [34, 35]. The exchange-correlation energy is determined via the Perdew-Burke-Ernzerhof (PBE) generalized gradient approximation (GGA) [36] using for Li and Zr the softer pseudopotential variants which treat p and s semi-core states as

valence states. Pure lithium lanthanum zirconate Li₇La₃Zr₂O₁₂ (LLZO) is substituted with different amounts of Al (x=0.125, 0.25, 0.375, 0.5, 0.625 and 0.75) and Ta (y=0.125, 0.25, 0.375, 0.5, 0.625 and 0.75), where the co-substituted LLZO results in Li_{7-3x-y}Al_xLa₃Zr_{2-y}Ta_yO₁₂ (Al_xTa_y:LLZO). The substitution of Li with Al creates a 3+ oxidation state, which leads to two more Li vacancies to achieve electrically neutral structures. However, the substitution of Li with Ta do not lead to more Li vacancies, but a Zr atom is replaced in the sense of electroneutrality. Due to the large set of possible substitution sites, preliminary screening calculations as explained in Ref. [17] are performed to reduce the configuration space drastically (see Fig. 1). We note that these four prescreening steps are optional, but improve efficiency and precision of the following calculations drastically. This electronic model is based on the calculation of the electrostatic energy via Ewald summation [37] and the pymatgen library [38], which provides various materials analysis features. Based on these estimates, ionic substitutions are made on sites which have the highest electrostatic energy, under consideration of the assigned oxidation states Li¹⁺, La³⁺, Zr⁴⁺, O²⁻, Al³⁺ and Ta⁵⁺.

The acceleration of the equilibrium atomic coordinates' determination can be beneficial for the reduction of the computational effort. Therefore, ML methods can replace the determination of the equilibrium structure in the calculation workflow. In this work we have developed an approach which takes guessed atomic coordinates as input values. As output, the trained ML algorithm delivers directly suggested equilibrium coordinates of the ions. To this end, we construct an artificial neural network (ANN), where the atomic Cartesian coordinates of each structure with different volumes are processed as input values (with maximum substitution level of Al x=0.5 and Ta y=0.375). Further details of the developed machine learning model will be presented elsewhere.

Additional preliminary ab initio simulations at the Γ point are performed for the five most energetically preferable configurations, selected via the described electronic model. Here, the energy cutoff is 550 eV and the stopping criteria for the electronic self-consistency loop is at 10^{-6} eV, while the ionic relaxation is stopped for forces smaller than 0.05 eV/Å. We note that all simulations are performed for fixed cell volume and cell shape but variable ionic positions, hence the ionic positions inside the cubic unit cell can relax during the DFT calculations for given volumes and deformations states of the cell.

The configuration with the lowest energy among the preliminary Γ point simulations is chosen for the productive calculations of the mechanical prop-

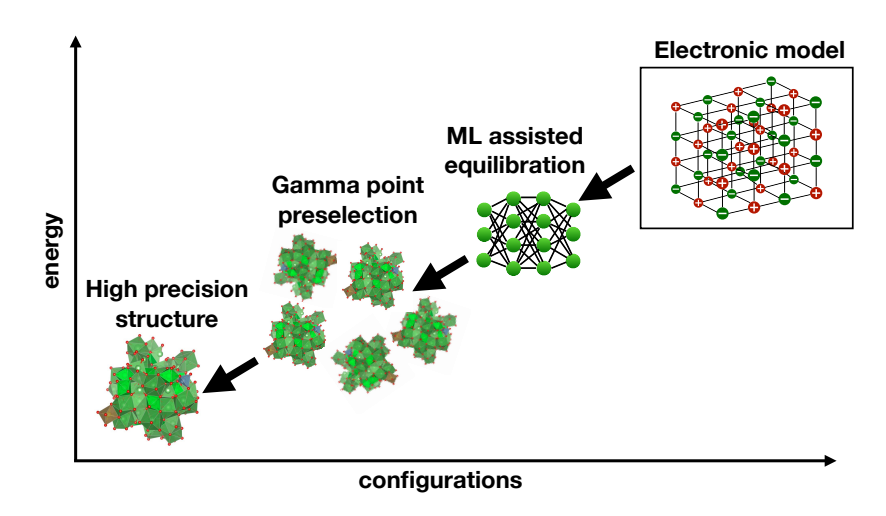


Figure 1: Illustration of the prescreening workflow. The large set of possible substitution sites is reduced via the electronic prescreening model to only five energetically favourable configurations, which can be pre-equilibrated via ML methods. Preliminary Γ point calculations determine the configuration with the lowest energy among the five structures. We note that this configuration is used for all following productive calculations, which include in particular a full k-point sampling.

erties. The simulation parameters are unchanged for the productive runs, except for the chosen energy cutoff of $700\,\mathrm{eV}$ and the $2\times2\times2$ mesh for the Brillouin zone, sampled using the Monkhorst-Pack scheme [39].

For the determination of mechanical properties, i.e. the elastic moduli in a cubic system, the knowledge of three elastic constants is required, and these elastic constants are calculated following the approach of Söderlind et al. [40]. First, the volume of the structures is varied isotropically for volume changes of up to $\pm 3\%$ and the resulting energy-volume curves are fitted with the Birch-Murnaghan equation of state [41, 42, 43] to determine the equilibrium volume and the bulk modulus of each structure. Next, the energy as function of a shear strain ϵ determines the three elastic constants in a cubic system, therefore the structures are deformed according to two

deformation matrices [40]

$$\mathbf{D}_{1} = \begin{pmatrix} 1 + \epsilon & 0 & 0 \\ 0 & 1 + \epsilon & 0 \\ 0 & 0 & 1/(1 + \epsilon)^{2} \end{pmatrix}, \tag{1}$$

$$\mathbf{D}_2 = \begin{pmatrix} 1 & \epsilon & 0 \\ \epsilon & 1 & 0 \\ 0 & 0 & 1/(1 - \epsilon^2) \end{pmatrix}, \tag{2}$$

where fitting allows to calculate the elastic constants via the tetragonal shear constant C' and bulk modulus B [40],

$$C' = \frac{1}{2}(C_{11} - C_{12}), (3)$$

$$B = \frac{1}{3}(C_{11} + 2C_{12}). (4)$$

With the knowledge of the elastic constants, i.e. C_{11} , C_{12} and C_{44} , we calculate the directional Young's modulus [21]

$$E_{[100]} = \frac{(C_{11} - C_{12})(C_{11} + 2C_{12})}{(C_{11} + C_{12})},$$

$$E_{[110]} = \frac{4(C_{11} - C_{12})(C_{11} + 2C_{12})C_{44}}{2C_{11}C_{44} + (C_{11} - C_{12})(C_{11} + 2C_{12})},$$

$$E_{[111]} = \frac{3(C_{11} + 2C_{12})C_{44}}{C_{11} + 2C_{12} + C_{44}},$$
(5)

and the shear modulus

$$G_{[100]} = C_{44},$$

$$G_{[110]} = \frac{2(C_{11} - C_{12})C_{44}}{C_{11} - C_{12} + 2C_{44}},$$

$$G_{[111]} = \frac{3(C_{11} - C_{12})C_{44}}{C_{11} - C_{12} + 4C_{44}}.$$
(6)

The comparison of these directional properties permits the evaluation of anisotropy of co-substituted LLZO. Additionally, we quantify the anisotropy of a cubic system via the Zener ratio [21]

$$A = \frac{2C_{44}}{C_{11} - C_{12}}. (7)$$

As for most battery related applications, polycrystalline LLZO with random grain orientations is used, we use homogenization models for the estimation of the isotropic material properties on the representative volume element scale. Therefore, the isotropic Voigt's shear modulus is used as upper bound [44, 45]

$$G_{\rm V} = \frac{1}{5}(C_{11} - C_{12} + 3C_{44}) \tag{8}$$

and the Voigt-Reuss-Hill averaging scheme involving upper and lower bound contributions [21]

$$G_{\text{VRH}} = \frac{1}{2} \left(\frac{C_{11} - C_{12} + 3C_{44}}{5} + \frac{5C_{44}(C_{11} - C_{12})}{4C_{44} + 3(C_{11} - C_{12})} \right). \tag{9}$$

These two estimates allow to get an impression of the range of elastic constants' variations within polycrystalline LLZO using different homogenization approaches. As will be shown below, the values are rather close to each other, and therefore the consideration of more sophisticated Hashin-Shtrikman bounds [46, 47] is not required.

Next, for an effectively isotropic polycrystalline material Young's modulus is estimated as [44, 45]

$$E = \frac{9BG_{\rm V}}{3B + G_{\rm V}}.\tag{10}$$

Afterwards, we determine Vicker's hardness via the following equation [48]

$$H_{\rm V} = 2(k^2 G_{\rm V})^{0.585} - 3, (11)$$

with $k = G_V/B$ being the ratio of shear and bulk modulus. This semiempirical model is based on Pugh's modulus ratio k and correlations between shear and bulk modulus and hardness, leading to an expression for $H_V = Ck^mG^n$, where the parameters C, m and n were previously determined by analyzing experimental data [48]. A good agreement between this theoretical model and experiments on LLZO was shown in [17].

The DFT calculations determine the elastic quantities at $0\,\mathrm{K}$, where an extrapolation of the values to room temperature (298 K) leads to more accurate comparisons with experiments. As proposed in [21] for increasing temperatures the elastic moduli of oxides decrease and a reduction by 5 % to mimic this decrease at 298 K can be applied.

We note that all results for the mechanical properties base on these described DFT calculations.

2.2. Differential effective medium theory

The pores appear on a scale which is larger than the electronic structure scale, therefore a scale bridging description is required. We employ a differential effective medium theory approach [49, 50] to capture the influence of pores on LLZO. As the polycrystalline material is effectively isotropic, also a random distribution of spherical pores does not influence the symmetry, and therefore we can describe the elastic response through e.g. Young's modulus and Poisson ratio alone. Specifically, the effective Young's modulus calculated via the differential effective medium theory is given by [31]

$$\frac{E_{\text{eff}}}{E} = \frac{3(c-1)^3[c(8\nu-2)(c^2-3c+3)-3(1+\nu)]}{(\nu+1)[c(4\nu-1)(c^2-3c+3)-3]^2},$$
(12)

which is expressed here in terms of the void concentration c and the Poisson ratio of the dense phase

$$\nu = \frac{3B - 2G_{\rm V}}{6B + 2G_{\rm V}},\tag{13}$$

using the upper bound of Voigt's shear modulus G_{V} .

3. Results

3.1. Mechanical properties

Following the steps described above, we calculate the elastic constants for different co-substituted LLZO structures via DFT simulations and determine the corresponding mechanical properties under the influence of high amounts of co-substitutions.

The mechanical properties of LLZO are determined via the calculation of the elastic constants. First, the comparison of the different values for the directional properties of Young's modulus and shear modulus, see equations (5) and (6), allows the evaluation of the co-substituted LLZO's anisotropy. The direction [111] shows the highest values of Young's modulus for all substitutions, whereas $E_{[100]}$ is lowest. The ratio between these directional contributions ranges from 1.13 to 1.36 for the different co-substituted configurations. The directional properties of the shear modulus exhibit similar ratios between 1.13 and 1.29, whereas the highest contribution belongs now to the [100] direction and the smallest to the direction [111]. The Zener anisotropy, see equation (7), allows the quantification of anisotropy in cubic systems, where a value of A=1 indicates isotropy. The highest value

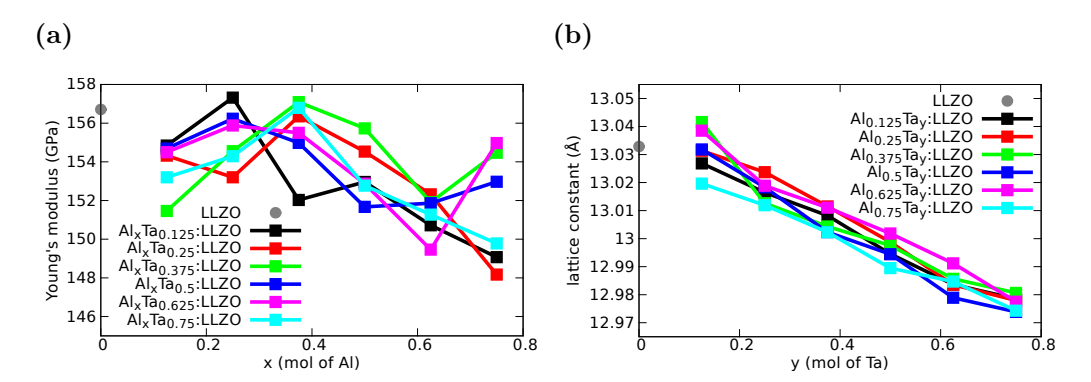


Figure 2: DFT calculated (a) Young's modulus and (b) lattice constant for different dopant configurations with (a) fixed Al and (b) fixed Ta concentrations. The grey point indicates the corresponding value for the unsubstituted structure in each plot. We note that this cubic structure is unstable at ambient temperatures.

A=1.44 is found in the single substituted $Al_{0.125}$:LLZO system, while the lowest value A=1.19 results for the co-substituted $Al_{0.625}$ Ta_{0.75}:LLZO structure. Overall, a decrease with increasing substitution level is visible, where the values for the Zener anisotropy range in the magnitude of other isotropic oxides like NiO (A=1.45) or MnO (A=1.54) [21]. Therefore, we expect that in polycristalline LLZO with random grain orientation, which is isotropic, the elastic properties will not deviate much from the averaged values. This is confirmed via a comparison of the upper bound of Voigt's shear modulus (Eq. 8) and the Voigt-Reuss-Hill averaging scheme (Eq. 9), where the deviations between both quantities are small. The highest difference ($G_V - G_{VRH}$)/ $G_{VRH} = 0.015$ between upper bound and average shear modulus is found for $Al_{0.125}$ Ta_{0.125}:LLZO, while the lowest difference is $(G_V - G_{VRH})/G_{VRH} = 0.002$ for $Al_{0.625}$ Ta_{0.625}:LLZO.

Fig. 2(a) shows the resulting Young's moduli as a function of Al content. The values of the co-substituted structures are smaller than the unsubstituted structure, except for Al_{0.125}Ta_{0.25}:LLZO and Al_{0.375}Ta_{0.25}:LLZO. For increasing Al level, the curves decrease slightly, however the variation of values for Young's modulus is small. We note in passing that the cubic and tetragonal phase have comparable Young's moduli, with a slighly higher value for the tetragonal phase, which is consistently found in experiments and simulation, see [17].

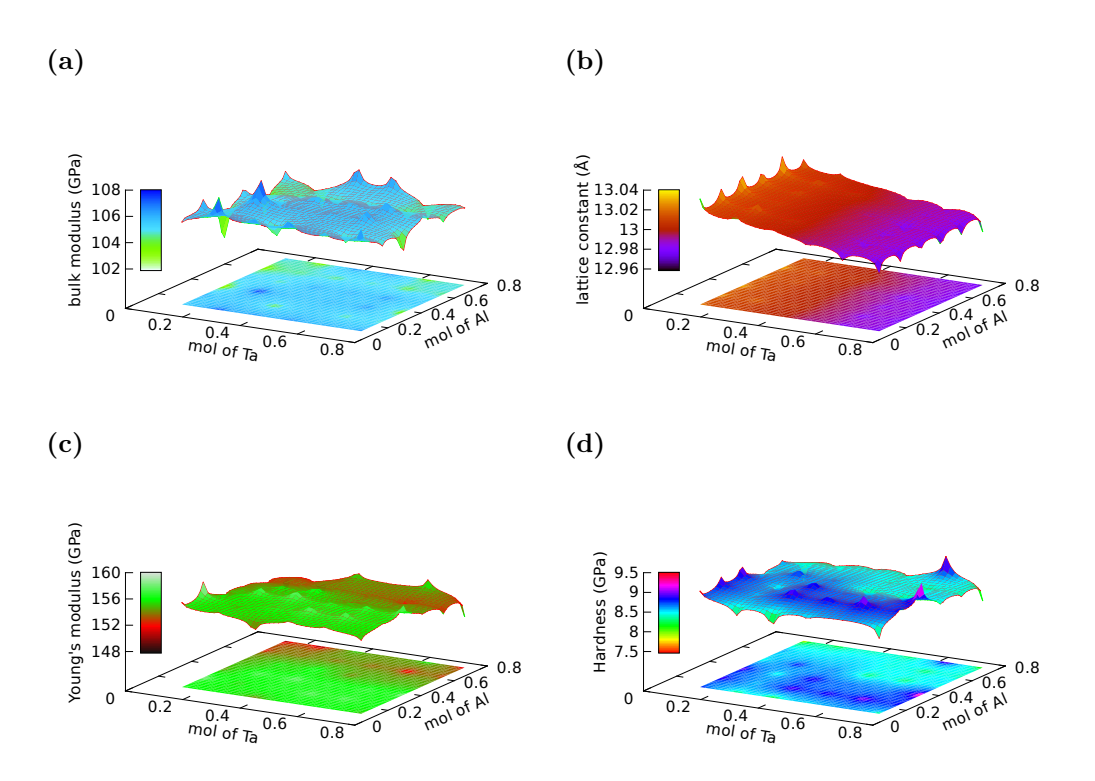


Figure 3: DFT calculated (a) bulk modulus, (b) lattice constant, (c) Young's modulus and (d) hardness for different dopant configurations in a 3D representation. The plots show that the mechanical properties of LLZO are preserved under substitutions with Al and Ta.

The 3D representation in Fig. 3(a) shows the resulting bulk moduli as a function of Ta and Al level. General, we expect a correlation between the lattice constants and elastic moduli, where smaller/higher bulk moduli lead to higher/smaller lattice constants due to weaker/stronger interatomic bonding, respectively [17]. This relationship is visible in our data, however the variation of data is again not very pronounced. Fig. 3(c) shows the resulting Young's modulus and confirms the previous finding, i.e. the decrease with increasing Al level.

Fig. 2(b) illustrates the resulting lattice constants as a function of substituted Ta content. It is clearly visible that the substitution of Ta has a higher influence on the lattice constant than Al substitutions. For low amounts

of Ta the resulting lattice constant lies in the regime of the unsubstituted structure, whereas for increasing Ta level the corresponding lattice constants decrease. The decrease of the lattice constants of structures with high Ta level is expected due to the smaller ionic radius of Ta compared to the substituted Zr [19]. We note that single substituted Al and Ta structures are calculated for benchmarking and the later comparison to the experimental data. For the single substituted Al_x :LLZO structures a higher lattice constant than for the unsubstituted structure is found, while for the Ta_x :LLZO structures smaller lattice constants are determined. This confirms the observed influence of Ta on the microstructural properties of co-substituted systems. These findings are also supported by the results of the theoretical and experimental investigation with single substitutions [17]. Overall, the variation of the lattice constants between the different co-substituted configurations is small and less than 0.1 Å. The 3D representation of the resulting mechanical properties in Fig. 3(b) reveals the same findings for the lattice constants, i.e. the decrease with increasing Ta level.

Finally, the calculated hardness, as illustrated in Fig. 3(d), shows again only a weak substitution dependence. All values are close to the unsubstituted structure.

3.2. Porous materials

LLZO used for typical battery applications is a porous material, whose pores have an influence on the mechanical properties. However, these effects cannot be captured via DFT calculations and therefore the differential effective medium theory is used as a scale bridging description. Generally, this approximation method shows a good agreement with the true effective elastic constants for low pore concentrations. For LLZO, the porosity is typically of the order of 10% [17], and therefore a sufficient accuracy of the predictions can be anticipated. Table 1 shows the resulting effective Young's modulus compared with corresponding experimental values and measured porosity data reported in [17]. We note that we extrapolate the simulated results to 298 K for a realistic comparison to the experiments. For dense, tetragonal LLZO without substitution, the computed and measured Young's moduli match. The unsubstituted, cubic structure results in a slightly smaller value for Young's modulus than the tetragonal counterpart.

As only for selected Ta content experimental elastic constants of pure cubic phase LLZO are available both for dense and porous samples, we restrict the comparisons to these cases. Here it should be mentioned that due

Substitution	Porosity	Young's modulus E	effective Young's modulus $E_{\rm eff}$
in $[\text{mol}\%]$	in [%]	in [GPa]	in [GPa]
Un-substituted			
$ ext{t-LLZO}^{ ext{exp}}$	23	156 ± 9	71 ± 3
$ ext{t-LLZO}^{ ext{sim}}$	23	155.3	71.1
$\rm LLZO^{sim}$	23	148.9	68.1
Ta-substituted			
$Ta_{0.125}$:LLZO sim	8	142.9	112.3
$Ta_{0.2}:LLZO^{exp}$	8	141 ± 2	117 ± 6
$Ta_{0.25}$:LLZO sim	8	144.9	112.8
$Ta_{0.375}$:LLZO ^{sim}	9	143.8	108.4
$Ta_{0.4}:LLZO^{exp}$	9	124 ± 3	82 ± 10

Table 1: Verification and comparison of the simulated, extrapolated results (superscript "sim") and experimental quantities (superscript "exp"), which are taken from [17], for single phase materials. All structures are cubic, except two tetragonal, unsubstituted configurations (prefix "t"). For the unsubstituted, tetragonal structure t-LLZO^{sim} the literature value $E=163.5\,\mathrm{GPa}$ (0 K) from [51] is used. All simulated values are extrapolated to 298 K (reduction of 5%), including the simulation literature value.

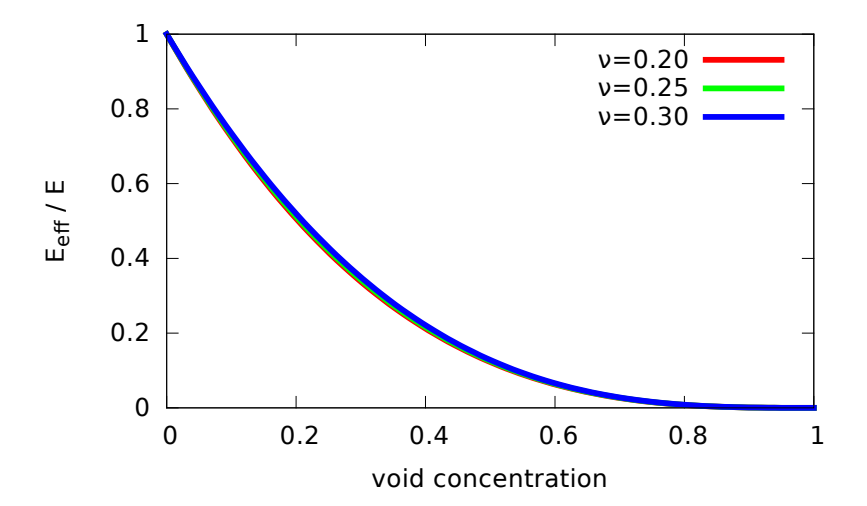


Figure 4: The decrease of the effective Young's modulus. The resulting ratio of the effective Young's modulus as function of the void concentration for different values of Poisson ratio ν , showing a very weak dependence on ν . We note that for an experimental expected porosity of 10% a decrease of 27% in the elastic quantities is expected.

to system size constraints, only specific Ta concentrations can be realized in the simulations, and we picked them to be as close as possible to the experimental compositions. The computed and extrapolated dense phase Young's moduli are similar to the experimental values with a deviation of the order of a few GPa, where only Ta_{0.4}:LLZO^{exp} is an outlier. For a porosity of around 10% we find a comparable drop of the effective Young's modulus both in simulations and experiments.

Fig. 4 shows the decrease of the ratio $E_{\rm eff}/E$ as function of the void concentration. Different values of the Poisson ratio ν do not affect the behavior of the elastic modulus decrease. Therefore, the expected LLZO porosity of around 10% leads to a decay by 27% of Young's modulus.

4. Conclusions

Ab initio DFT simulations of garnet structured Li₇La₃Zr₂O₁₂ with cosubstitutions of Al and Ta are performed and elastic constants and further structural and mechanical properties are calculated.

LLZO shows a pronounced dependence on the Ta substitution level due to the smaller ionic radius of Ta. Also, for the Young's modulus a slight dependency on the Al content is found, while the values for the resulting hardness range in the order of magnitude of the unsubstituted structure. The co-substitutions preserve the structural and mechanical properties, which is important regarding the fabrication of batteries using LLZO.

The differential effective medium theory allows the inclusion of pores and bridges the gap towards application relevant materials. Benchmarking and validation of our simulation results with single substituted experimental values shows a good agreement and allows the usage of our model for consistency checks of experimental and theoretical results. The porosity of LLZO lies at around 10~% and this leads to an expected decay of 27~% for Young's modulus.

Overall, the presented scale bridging calculations lead to reliable predictions of the mechanical properties of doped LLZO. The obtained results can be useful for the optimization of the mechanical behavior of the solid electrolyte as well as a beneficial mechanical matching to the electrodes to potentially improve electrical contacting and to contribute to the suppression of dendrite formation.

CRediT authorship contribution statement

Roland Sandt: Conceptualization, Methodology, Software, Validation, Formal analysis, Investigation, Visualization, Writing - Original Draft, Review & Editing Yaxue Wang: Formal analysis, Investigation, Data Curation Robert Spatschek: Conceptualization, Writing - Review & Editing, Supervision, Project administration, Funding acquisition

Declaration of Competing Interest

The authors declare no competing financial or non-financial interests.

Data availability

Data will be made available on request.

Acknowledgements

This research was funded by the German Federal Ministry of Education and Research (BMBF) via the project Meet HiEnD 3 and the Helmholtz project ZeDaBase. Open access was funded by the Deutsche Forschungsgemeinschaft (DFG, German Research Foundation) - 491111487. The authors gratefully acknowledge the computing time granted by the JARA Vergabegremium and provided on the JARA Partition part of the supercomputer JURECA at Forschungszentrum Jülich [52].

References

- [1] J.-F. Wu, W. K. Pang, V. K. Peterson, L. Wei, X. Guo, Garnet-Type Fast Li-Ion Conductors with High Ionic Conductivities for All-Solid-State Batteries, ACS Appl. Mater. Interfaces 9 (2017) 12461–12468. doi:https://doi.org/10.1021/acsami.7b00614.
- [2] J. Janek, W. G. Zeier, A solid future for battery development, Nature Energy 1 (2016) 16141. doi:https://doi.org/10.1038/nenergy.2016.141.
- [3] Q. Liu, L. Jiang, P. Zheng, J. Sun, C. Liu, J. Chai, X. Li, Y. Zheng, Z. Liu, Recent Advantages in Stability Issues of Inorganic Solid Electrolytes and Composite Solid Electrolytes for All-Solid-State Batteries, Chem. Rec. 22 (2022) e202200116. doi:https://doi.org/10.1002/tcr.202200116.

- [4] C. Wang, K. Fu, S. P. Kammampata, D. W. McOwen, A. J. Samson, L. Zhang, G. T. Hitz, A. M. Nolan, E. D. Wachsman, Y. Mo, V. Thangadurai, L. Hu, Garnet-Type Solid-State Electrolytes: Materials, Interfaces, and Batteries, Chem. Rev. 120 (2020) 4257–4300. doi:https://doi.org/10.1021/acs.chemrev.9b00427.
- [5] S. Kim, J.-S. Kim, L. Miara, Y. Wang, S.-K. Jung, S. Y. Park, Z. Song, H. Kim, M. Badding, J. Chang, V. Roev, G. Yoon, R. Kim, J.-H. Kim, K. Yoon, D. Im, K. Kang, High-energy and durable lithium metal batteries using garnet-type solid electrolytes with tailored lithium-metal compatibility, Nature Communications 13 (2022) 1883. doi:https://doi.org/10.1038/s41467-022-29531-x.
- [6] R. Koerver, W. Zhang, L. de Biasi, S. Schweidler, A. O. Kondrakov, S. Kolling, T. Brezesinski, P. Hartmann, W. G. Zeier, J. Janek, Chemomechanical expansion of lithium electrode materials - on the route to mechanically optimized all-solid-state batteries, Energy Environ. Sci. 11 (2018) 2142. doi:https://doi.org/10.1039/C8EE00907D.
- [7] G. McConohy, X. Xu, T. Cui, E. Barks, S. Wang, E. Kaeli, C. Melamed, X. W. Gu, W. C. Chueh, Mechanical regulation of lithium intrusion probability in garnet solid electrolytes, Nature Energy (2023). doi:https://doi.org/10.1038/s41560-022-01186-4.
- [8] Y. Chen, Y. Jiang, S.-S. Chi, H. J. Woo, K. Yu, J. Wang, C. Wang, Y. Deng, Understanding the dendrites garnet-based solid-state lithiumgrowth in metal batteries. Journal of Power Sources (2022)230921. doi:https://doi.org/10.1016/j.jpowsour.2021.230921.
- [9] S. Fu, Y. Arinicheva, C. Hüter, M. Finsterbusch, R. Spatschek, Grain Boundary Characterization and Potential Percolation of the Solid Electrolyte LLZO, Batteries 9 (2023) 222. doi:https://doi.org/10.3390/batteries9040222.
- [10] C. D. Fincher, C. E. Athanasiou, C. Gilgenbach, M. Wang, B. W. Sheldon, W. C. Carter, Y.-M. Chiang, Controlling dendrite propagation in solid-state batteries with engineered stress, Joule 6 (2022) 2794–2809. doi:https://doi.org/10.1016/j.joule.2022.10.011.

- [11] R. Murugan, V. Thangadurai, W. Weppner, Fast Lithium Ion Conduction in Garnet-Type Li₇La₃Zr₂O₁₂, Angew. Chem. Int. Ed. 46 (2007) 7778–7781. doi:https://doi.org/10.1002/anie.200701144.
- [12] C. A. Geiger, E. Alekseev, B. Lazic, M. Fisch, T. Armbruster, R. Langner, M. Fechtelkord, N. Kim, T. Pettke, W. Weppner, Crystal Chemistry and Stability of "Li₇La₃Zr₂O₁₂" Garnet: A Fast Lithium-Ion Conductor, Inorganic Chemistry 50 (2011) 1089–1097. doi:https://doi.org/10.1021/ic101914e.
- [13] E. Enkhbayar, J. H. Kim, Study of Codoping Effects of Ta^{5+} and Ga^{3+} on Garnet $\mathrm{Li}_7\mathrm{La}_3\mathrm{Zr}_2\mathrm{O}_{12}$, ACS Omega 7 (2022) 47265–47273. doi:https://doi.org/10.1021/acsomega.2c06544.
- [14] L. J. Miara, S. P. Ong, Y. Mo, W. D. Richards, Y. Park, J.-M. Lee, H. S. Lee, G. Ceder, Effect of Rb and Ta Doping on the Ionic Conductivity and Stability of the Garnet Li_{7+2x-y} (La_{3-x} Rb_x) (Zr_{2-y} Ta_y) O₁₂ ($0 \le x \le 0.375, 0 \le y \le 1$) Superionic Conductor: A First Principles Investigation, Chem. Mater. 25 (2013) 3048–3055. doi:https://doi.org/10.1021/cm401232r.
- [15] H. Buschmann, J. Dölle, S. Berendts, A. Kuhn, P. Bottke, M. Wilkening, P. Heitjans, A. Senyshyn, H. Ehrenberg, A. Lotnyk, V. Duppel, L. Kienle, J. Janek, Structure and dynamics of the fast lithium ion conductor "Li₇La₃Zr₂O₁₂", Phys. Chem. Chem. Phys. 13 (2011) 19378–19392. doi:https://doi.org/10.1039/C1CP22108F.
- [16] A.-N. Wang, J. F. Nonemacher, G. Yan, M. Finsterbusch, J. Malzbender, M. Krüger, Mechanical properties of the solid electrolyte Alsubstituted Li₇La₃Zr₂O₁₂ (LLZO) by utilizing micro-pillar indentation splitting test, Journal of the European Ceramic Society 38 (2018) 3201–3209. doi:https://doi.org/10.1016/j.jeurceramsoc.2018.02.032.
- [17] J. F. Nonemacher, C. Hüter, H. Zheng, J. Malzbender, M. Krüger, R. Spatschek, M. Finsterbusch, Microstructure and properties investigation of garnet structured Li₇La₃Zr₂O₁₂ as electrolyte for all-solid-state batteries, Solid State Ionics 321 (2018) 126–134. doi:https://doi.org/10.1016/j.ssi.2018.04.016.

- [18] A. Kuhn, J.-Y. Choi, L. Robben, F. Tietz, M. Wilkening, P. Heitjans, Li Ion Dynamics in Al-Doped Garnet-Type Li₇La₃Zr₂O₁₂ Crystallizing with Cubic Symmetry, Z. Phys. Chem. 226 (2012) 525–537. doi:https://doi.org/10.1524/zpch.2012.0250.
- [19] Y. Wang, W. Lai, High Ionic Conductivity Lithium Garnet Oxides of Li_{7-x}La₃Zr_{2-x}Ta_xO₁₂ Compositions, Electrochem. Solid-State Lett. 15 (2012) A68. doi:DOI 10.1149/2.024205esl.
- [20] D. O. Shin, K. Oh, K. M. Kim, K.-Y. Park, B. Lee, Y.-G. Lee, K. Kang, Synergistic multi-doping effects on the Li₇La₃Zr₂O₁₂ solid electrolyte for fast lithium ion conduction, Scientific Reports 5 (2015) 18053. doi:https://doi.org/10.1038/srep18053.
- [21] S. Yu, R. D. Schmidt, R. Garcia-Mendez, E. Herbert, N. J. Dudney, J. B. Wolfenstine, J. Sakamoto, D. J. Siegel, Elastic Properties of the Solid Electrolyte Li₇La₃Zr₂O₁₂ (LLZO), Chem. Mater. 28 (2016) 197–206. doi:https://doi.org/10.1021/acs.chemmater.5b03854.
- [22] B. Celik, R. Sandt, L. C. Pereira dos Santos, R. Spatschek, Prediction of Battery Cycle Life Using Early-Cycle Data, Machine Learning and Data Management, Batteries 8 (2022) 266. doi:https://doi.org/10.3390/batteries8120266.
- [23] O. I. Abiodun, A. Jantan, A. E. Omolara, K. V. Dada, N. A. Mohamed, H. Arshad, State-of-the-art in artificial neural network applications: A survey, Heliyon 4 (2018) e00938. doi:https://doi.org/10.1016/j.heliyon.2018.e00938.
- [24] D. Yang, Y. Wang, R. Pan, R. Chen, Z. Chen, A neural network based state-of-health estimation of lithium-ion battery in electric vehicles, Energy Procedia 105 (2017) 2059–2064. doi:https://doi.org/10.1016/j.egypro.2017.03.583.
- [25] H. Wen, C. Huang, S. Guo, The Application of Convolutional Neural Networks (CNNs) to Recognize Defects in 3D-Printed Parts, Materials 14 (2021) 2575. doi:https://doi.org/10.3390/ma14102575.
- [26] R. Jinnouchi, J. Lahnsteiner, F. Karsai, G. Kresse, M. Bokdam, Phase Transitions of Hybrid Perovskites Simulated

- by Machine-Learning Force Fields Trained on the Fly with Bayesian Inference, Physical Review Letters 122 (2019) 225701. doi:https://doi.org/10.1103/PhysRevLett.122.225701.
- [27] M. Bogojeski, L. Vogt-Maranto, M. E. Tuckerman, K.-R. Müller, K. Burke, Quantum chemical accuracy from density functional approximations via machine learning, Nature Communications 11 (2020) 5223. doi:https://doi.org/10.1038/s41467-020-19093-1.
- [28] G. Hegde, R. C. Bowen, Machine-learned approximations to Density Functional Theory Hamiltonians, Scientific Reports 7 (2017) 42669. doi:https://doi.org/10.1038/srep42669.
- [29] M. Fronzi, R. D. Amos, R. Kobayashi, N. Matsumura, K. Watanabe, R. K. Morizawa, Evaluation of Machine Learning Interatomic Potentials for the Properties of Gold Nanoparticles, Nanomaterials 12 (2022) 3891. doi:https://doi.org/10.3390/nano12213891.
- [30] M. Hodapp, A. Shapeev, Machine-learning potentials able predictive and tractable high-throughput screening Phys. Rev. Materials random alloys, (2021)doi:https://doi.org/10.1103/PhysRevMaterials.5.113802.
- [31] R. Spatschek, C. Gugenberger, E. A. Brener, Effective elastic moduli in solids with high density of cracks, Physical Review B 80 (2009) 144106. doi:https://doi.org/10.1103/PhysRevB.80.144106.
- [32] A. R. Day, K. A. Snyder, E. J. Garboczi, M. F. Thorpe, The elastic moduli of a sheet containing circular holes, J. Mech. Phys. Solids 40 (1992) 1031–1051. doi:https://doi.org/10.1016/0022-5096(92)90061-6.
- [33] G. Kresse, J. Furthmüller, Efficient iterative schemes for *ab initio* totalenergy calculations using a plane-wave basis set, Physical Review B 54 (1996) 11169. doi:https://doi.org/10.1103/PhysRevB.54.11169.
- [34] P. E. Blöchl, Projector augmented-wave method, Physical Review B 50 (1994) 17953. doi:https://doi.org/10.1103/PhysRevB.50.17953.
- [35] G. Kresse, D. Joubert, From ultrasoft pseudopotentials to the projector augmented-wave method, Physical Review B 59 (1999) 1758. doi:https://doi.org/10.1103/PhysRevB.59.1758.

- [36] J. P. Perdew, K. Burke, M. Ernzerhof, Generalized Gradient Approximation Made Simple, Physical Review Letters 77 (1996) 3865. doi:https://doi.org/10.1103/PhysRevLett.77.3865.
- [37] P. P. Ewald, Die Berechnung optischer und elektrostatischer Gitterpotentiale, Annalen der Physik 369 (1921) 253–287. doi:https://doi.org/10.1002/andp.19213690304.
- [38] S. P. Ong, W. D. Richards, A. Jain, G. Hautier, M. Kocher, S. Cholia, D. Gunter, V. L. Chevrier, K. A. Persson, G. Ceder, Python Materials Genomics (pymatgen): A robust, open-source python library for materials analysis, Computational Materials Science 68 (2012) 314–319. doi:https://doi.org/10.1016/j.commatsci.2012.10.028.
- [39] H. J. Monkhorst, J. D. Pack, Special points for Brillouinzone integrations, Physical Review B 13 (1976) 5188. doi:https://doi.org/10.1103/PhysRevB.13.5188.
- [40] P. Söderlind, O. Eriksson, J. M. Wills, A. M. Boring, Theory of elastic constants of cubic transition metals and alloys, Physical Review B 48 (1993) 5844–5851. doi:https://doi.org/10.1103/PhysRevB.48.5844.
- [41] F. D. Murnaghan, The Compressibility of Media under Extreme Pressures, Proc. Natl. Acad. Sci. USA 30 (1944) 244–247. doi:https://doi.org/10.1073/pnas.30.9.244.
- [42] F. Birch, Finite Elastic Strain of Cubic Crystals, Physical Review 71 (1947) 809–824. doi:https://doi.org/10.1103/PhysRev.71.809.
- [43] C. Hüter, M. Friák, M. Weikamp, J. Neugebauer, N. Goldenfeld, B. Svendsen, R. Spatschek, Nonlinear elastic effects in phase field crystal and amplitude equations: Comparison to ab initio simulations of bcc metals and graphene, Physical Review B 93 (2016) 214105. doi:https://doi.org/10.1103/PhysRevB.93.214105.
- [44] X. Li, J. Zhao, J. Xu, Mechanical properties of bcc Fe-Cr alloys by first-principles simulations, Front. Phys. 7 (2012) 360–365. doi:https://doi.org/10.1007/s11467-011-0193-0.

- [45] M. Jamal, S. Jalalil Asadabadi, I. Ahmad, H. A. Rahnamaye Aliabad, Elastic constants of cubic crystals, Computational Materials Science 95 (2014) 592–599. doi:https://doi.org/10.1016/j.commatsci.2014.08.027.
- [46] Z. Hashin, S. Shtrikman, A variational approach to the theory of the elastic behaviour of polycrystals, J. Mech. Phys. Solids 10 (1962) 343–352. doi:https://doi.org/10.1016/0022-5096(62)90005-4.
- [47] Z. Hashin, S. Shtrikman, A variational approach to the theory of the elastic behaviour of multiphase materials, J. Mech. Phys. Solids 11 (1963) 127–140. doi:https://doi.org/10.1016/0022-5096(63)90060-7.
- [48] X.-Q. Chen, H. Niu, D. Li, Y. Li, Modeling hardness of polycrystalline materials and bulk metallic glasses, Intermetallics 19 (2011) 1275–1281. doi:https://doi.org/10.1016/j.intermet.2011.03.026.
- [49] D. A. G. Bruggeman, Berechnung verschiedener physikalischer Konstanten von heterogenen Substanzen. I. Dielektrizitätskonstanten und Leitfähigkeiten der Mischkörper aus isotropen Substanzen, Ann. Phys. 416 (1935) 636–664. doi:https://doi.org/10.1002/andp.19354160705.
- [50] S. Nemat-Nasser, M. Hori, Micromechanics: Overall Properties of Heterogeneous Materials, 2nd ed., North-Holland, Amsterdam, 1998.
- [51] R. Maphoto, M. Masedi, P. Ngoepe, R. Ledwaba, First-principles study on structural, mechanical and electronic properties of Li₇La₃Zr₂O₁₂ solid electrolyte, Suid-Afrikaans Tydskrif vir Natuurwetenskap en Tegnologie South African Journal of Science and Technology 40 (2022) 12–15. doi:https://doi.org/10.36303/SATNT.2021cosaami.03.
- [52] Jülich Supercomputing Centre, JURECA: Data Centric and Booster Modules implementing the Modular Supercomputing Architecture at Jülich Supercomputing Centre, J. Large-scale Res. Facilities 7 (2018) A182. doi:10.17815/jlsrf-7-182.